THE EUROPEAN
PHYSICAL JOURNAL C

Regular Article - Experimental Physics

Development of a semi-cylindrical time projection chamber prototype for (^{3}He, t) charge exchange reaction experiment

Zhixuan He[1], **Meng Li[2,a]**, **Wenjuan Bu[1]**, **Chaoyuan Xiao[3]**, **Xianglun Wei[4,5]**, **Yuansheng Yang[4,5]**, **Zhi Qin[6]**, **Shanhaowei He[1]**, **Tianli Qiu[4,5]**, **Peng Ma[4,5]**, **Chengui Lu[4,5]**, **Limin Duan[4,5]**, **Bitao Hu[1]**, **Yi Zhang[1]**, **Herun Yang[4,5,b]**

[1] School of Nuclear Science and Technology, Lanzhou University, Lanzhou 730000, Gansu, China
[2] Department of Oncology, The Second Xiangya Hospital of Central South University, Changsha 410011, Hunan, China
[3] China Nuclear Power Technology Research Institute Co., Ltd., Shenzhen 518000, Guangdong, China
[4] Institute of Modern Physics, Chinese Academy of Sciences, Lanzhou 730000, Gansu, China
[5] School of Nuclear Science and Technology, University of Chinese Academy of Sciences, Beijing 100049, China
[6] Department of Physics, Tsinghua University, Beijing 100084, China

Abstract The charge exchange (CE) reaction is an effective probe to study the structure of atomic nuclei in the isospin dimension, which has been studied for decades. To expand the range of nuclei studied by CE reactions to a wider range and research the structure characteristics of unstable nuclei, including the isospin symmetry, spin-isospin excitation, and nuclear symmetry energy, a semi-cylindrical time projection chamber (scTPC) prototype was designed and constructed to probe (^{3}He,t) CE reactions in inverse kinematics. The 266 nm UV laser was used to achieve electron-drift-velocity calibration. The scTPC has an energy resolution (FWHM) of 5.6% for α particles emitted by ^{241}Am radioactive source. The position resolution of scTPC is described by the *residual* method. The spatial resolution on the pad plane is 409 μm. And the position resolution in the drift direction is 326 μm, equivalent to an angular resolution of 0.4°. These performances suggest that the scTPC can measure ΔE and particle tracks precisely. The successful development of the scTPC prototype provides better conditions for the next step of experimental data analysis and processing.

1 Introduction

The charge exchange (CE) reaction offers the possibility to explore the formation of the intrinsic structure of the nucleus, related to the excitation inducing isospin flip (with possibly also spin flip) [1–3]. CE reactions, e.g., (p,n), (^{3}He,t), and (t,^{3}He), with hadronic probes, are able to map the Gamow–Teller (G-T) response which is beyond the energy window accessible by β decay and difficult to achieve by direct measurements with neutrinos [2]. Besides, the CE scattering to the isobaric analog state (IAS) mediated by the Fermi transition, which is considered as the 'elastic' scattering, can serve as a probe for studying the neutron skin and symmetry energy of nuclear matter [4].

Theoretical and experimental research on the CE reaction has advanced significantly since the last century. Several CE reactions experiments involving (^{3}He,t) and (t,^{3}He) reactions have been conducted at the Indiana University Cyclotron Facility (IUCF) [5], National Superconducting Cyclotron Laboratory (NSCL) at Michigan State University, and Research Center for Nuclear Physics (RCNP) at Osaka University [3,6–10] using the ^{3}He or triton beam to bombard targets (e.g., ^{12,13}C, ^{16}O, ^{24,26}Mg, ^{28}Si, ^{40}Ca, ^{58,60}Ni, ^{90}Zr, ^{136}Xe, ^{76}Ge, ^{128,130}Te, etc.). The structure of the nucleus and the process of nuclear reaction, including the giant dipole resonance (GDR), double-β-decay nucleus, weak interaction strength, etc. are intensively studied by these groups. It is important for further study such calculations by comparing G-T transition and Fermi transition strength up to high excitation energies and expanding the range of nuclei studied to a wider range, such as the halo nuclei and nuclear drip lines, CE reactions in inverse kinematics are excellent tools for those purposes. For CE reactions in inverse kinematics, the detection with high efficiency and acceptance is a daunting technical challenge but also presents exciting opportunities for scientific breakthroughs [11,12]. The development of CE reaction experiments in inverse kinematics will facilitate a deeper understanding of the structure and properties of

unstable nuclei, especially with respect to the halo and shell structure of nuclei.

We presented a (^{3}He,t) Charge Exchange Reaction Detector (CERD) prototype (see Fig. 1) to validate the feasibility of measuring the (^{3}He,t) CE reaction in inverse kinematics with the heavy-ion beam of the Heavy Ion Research Facility in Lanzhou (HIRFL) at the Institute of Modern Physics (IMP) [13]. In order to achieve this type of (^{3}He,t) experiment, it is necessary to operate the TPC as a tracking medium to reconstruct the missing mass energy and the scattering angle of the triton. The design of the CERD allows for an expanded range of nuclei studied via CE reactions, particularly for unstable nuclei close to the neutron drip line, which are less explored in previous work. The prototype detector is based on $\Delta E - E$ telescope with both good energy and angular resolution to investigate particles with different emission angles, consisting of a semi-cylindrical time projection chamber (scTPC, see the green volume in Fig. 1), an array of CsI(Tl) scintillators (the gray array in Fig. 1), front-end electronics, and data acquisition system. The particular design consideration with a semi-cylindrical shape was given to realize an efficient detection of the large-scale CE reaction in inverse kinematics for the polarized-^{3}He experiment. The space on the top of the detector is needed for the installation of the future polarization devices (similar to schematic view of the ^{3}He glass cell in Ref. [14]). It is difficult to design a chamber with a semi-cylindrical structure because the electric field uniformity in the sensitive region significantly determines energy resolution and the three-dimensional position resolution of the time projection chamber (TPC). A special external structural bracing frame was designed to ensure structural stability. The feasibility of the scheme was confirmed through measurements with the laser and ^{241}Am radioactive source. The 266 nm UV laser was used to achieve electron-drift-velocity calibration. And the α source was used to measure the energy and spatial resolutions of the detector. In general, the scTPC has good performance and can support the development of CE reaction experiments.

This article focuses on the design, assembly, and performance testing of the scTPC. The design and setup of the scTPC are described in Sect. 2. The performance test and result are discussed in Sect. 3. The discussion about the simulation and beam experiment related to the CE reaction are described in Sect. 4. The conclusion and perspectives of future experiments are pointed out in Sect. 5.

2 Design and setup of scTPC

The CE reaction product of interest is triton (t). And the byproducts proton (p), deuteron (d), ^{3}He, and α particles may be generated during the bombardment. The $\Delta E - E$ telescope, where the scTPC is the ΔE detector and the CsI(Tl)
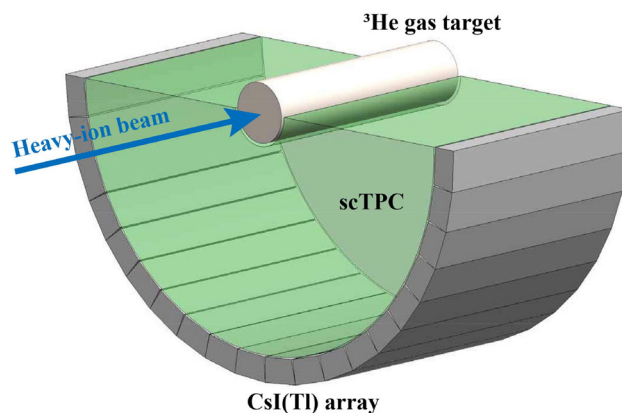
Fig. 1 Design schematic view of the CERD prototype detector. The blue line is the heavy-ion beam. The white tube is the ^{3}He gas target, the green volume is the scTPC, and the gray array is the CsI(Tl) scintillators

array serves as the E detector, can achieve particle identification (PID).

For effective measurement of CE reactions, the energy dynamic range and size of the detector were determined through the calculation and simulation firstly. The TPC was chosen as our ΔE detector, because the TPC is widely used in nuclear and particle physics experiments, allowing for the reconstruction of the charged particle's three-dimensional track and measure of the deposited energy precisely [15–22]. Our scTPC is based on the thick gas electron multiplier (THGEM) due to its advantages, such as durability, affordability, and versatility in terms of shape and size [23–27].

2.1 Kinematic estimation and Monte Carlo simulation

Complete kinematics measurements help to provide a strong selectivity of the reaction mechanism and also reduce significantly the background in the experimental data. As the first step, we must consider the kinematic range for (^{3}He,t) charge exchange reactions in inverse kinematics. Neglecting the excitation energy, the CE reaction can be regarded as the elastic scattering [28,29]. The energy and scattering angle (θ) of the recoiled t are closely related, at an energy of 500 MeV/nucleon ^{17}C and ^{3}He target, as shown in Fig. 2, calculated with the Kinematic calculator (relativistic) of LISE++ [30,31]. We focus on the large angle scattering region of the laboratory frame in inverse kinematics, that is, the small angle region in the center-of-mass frame, which has rich physical information, and the angular-momentum transfer q is small and tends to zero [2,3]. In this angle region, the kinetic energy of the recoiled t is in the range of tens of MeV to hundreds of MeV. And the triton with high kinetic energies requires a thick layer of CsI(Tl) scintillator for complete deposition.

We developed a Monte Carlo simulation package utilizing the Geant4 [32–34] to determine the structure of the detec-
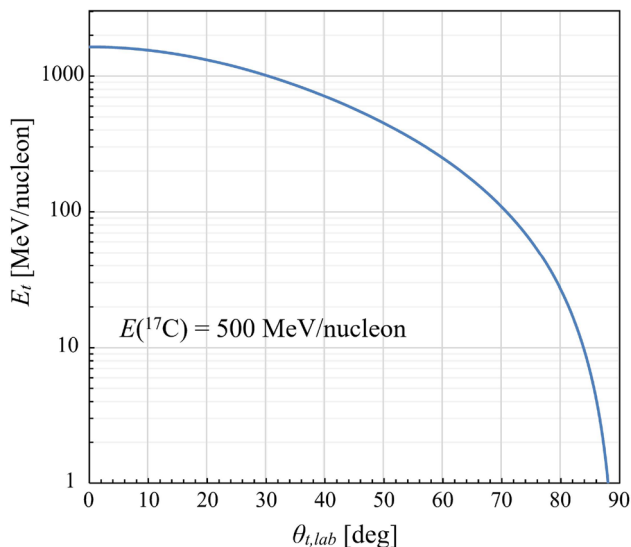
Fig. 2 Calculated energy versus scattering angle of triton

tion system (see Sect. 2.2 for detailed dimensions and design of the detector). The model constructed by Geant4 is shown as Fig. 1. The white cylinder in the center is the ^{3}He gas at 3 atmospheres with a diameter of 3 cm. The ^{3}He gas is encapsulated by a stainless-steel chamber with a 200 µm thick sidewall. The centers of the ^{3}He target and the TPC coincide on the same axis. The TPC sensitive volume with an external radius of 20 cm and CsI(Tl) scintillator with a thickness of 2 cm were determined after we weighed the kinematic range studied and cost. The TPC consists of two parts: the sensitive gas and field cage. The sensitive gas is located inside the field cage. The field cage substrate is FR4 material with a thickness of 0.66 mm and both sides of the substrate were covered with 0.02 mm thick copper. The green space inside the field cage is filled with the Ar (95%) + iC$_4$H$_{10}$ (5%) gas at one atmosphere. The outermost gray volume is CsI(Tl), which is covered with a 0.135 mm thick Teflon reflective layer. The triton and other byproducts were generated directly to observe the energy range limited by the detector's size. To keep things simple, various particles follow the correlation between the energy and ejection angle of the triton as shown in Fig. 2. Assuming a typical energy resolution of 10% for the scTPC and 8% for the scintillator, the simulated ΔE–E distribution is shown in Fig. 3(a). The triton can be distinguished from other byproducts clearly. The triton emitted at low kinetic energies (no more than 20 MeV) is often absorbed completely by the target, target's container and inner field cage, shown as Fig. 3(b). The maximal energy of triton that can be probed is about 140 MeV, decided by the thickness of 2 cm thick CsI(Tl). The energy loss for the triton in the gas volume of the scTPC is about 0.2 ∼ 1.0 MeV. Therefore, we believe that the detector is suitable for measuring t with the scattering angle of about 76° ∼

85°, in which the kinetic energy is about 20 ∼ 140 MeV, according to Fig. 2. Furthermore, this simulation result can be applied to achieve PID in the data analysis after the beam experiment.

2.2 General design of scTPC

In outline, the scTPC consists of a hollow semi-cylinder whose axis is aligned with the beam from the radioactive ion beam line. The scTPC is designed to cover up to 2π sr solid angle at most, with the upper part reserved for a polarization equipment system for the future ^{3}He target. The scTPC consists of four main components: a cathode, a field cage, two layers of THGEM foils, and a readout board, shown as Fig. 4(a). The length of the scTPC, from the lower surface of the cathode to the upper surface of the THGEM, is 200 mm. The inner and outer radii of the scTPC are 25 mm and 197 mm, respectively, shown as Fig. 4(b). The cathode is an FR4 copper clad board. The drift region length of the scTPC is 198 mm, while the transfer gap between the double THGEM foils is 2 mm. Additionally, the depth of the induction region is also 2 mm, shown as Fig. 4(c).

The charged particle passes through the gas volume and produces a series of primary ionization along the particle's track. The primary ionization electrons drift towards the THGEM driven by the electric field in the cage. The electron signals are amplified by THGEM foils, which are collected by the two-dimensional readout pads. The response of the readout pads to signals can reconstruct the projection in the plane of the readout board (x–y plane) of the three-dimensional track. The projection in the drift direction (z direction) of the track can be inferred from the ionized electrons' drift time and velocity, which is closely related to the ejection angles of the reaction products. In addition to the three-dimensional track, the energy loss of the charged particle in the gas volume, which will be utilized to achieve PID by the ΔE–E telescope, can be measured by the scTPC precisely as well.

The scTPC is housed in a dedicated vacuum chamber, which was designed to provide mechanical support and electromagnetic shielding of the detector, shown as Fig. 4(**d**). The gas mixture is Ar (95%) + iC$_4$H$_{10}$ (5%). This gas mixture can achieve high gain with the lower applied voltage between the electrodes of THGEM. In practice, due to physical constraints, only about a 70° range in the circumferential direction is utilized as an effective sensitive region in this prototype (see Sect. 2.5).

2.3 THGEM

The scTPC employs two layers of THGEM foils that were designed by us and manufactured by the University of Science and Technology of China (USTC) [35], shown as Fig. 5.
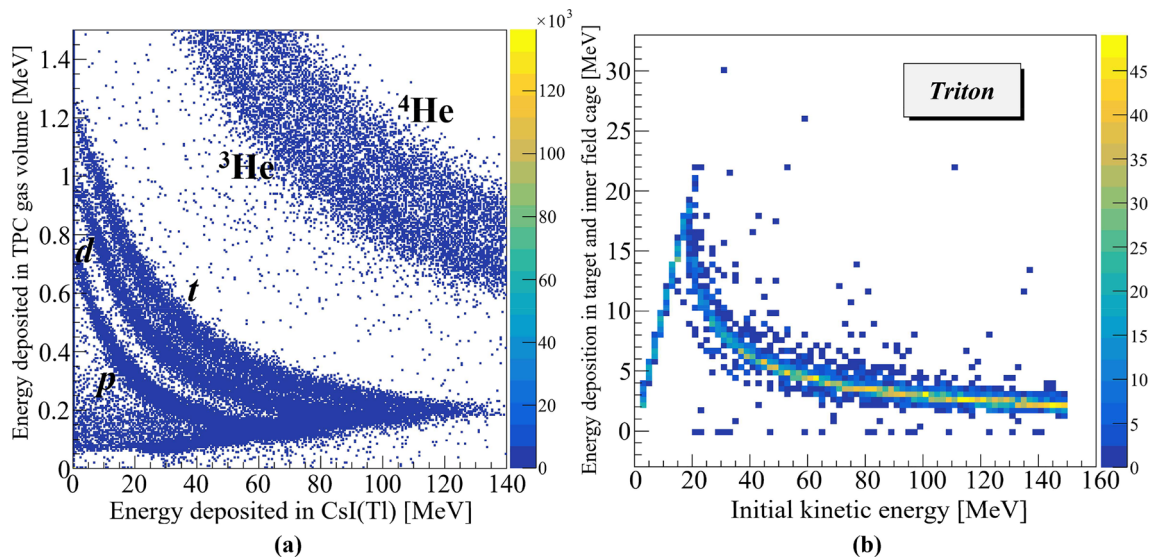
Fig. 3 Simulated $\Delta E - E$ distribution of the detection system (**a**) and energy loss in ^{3}He gas, stainless steel sidewall and inner field cage versus initial kinetic energy of triton (**b**)
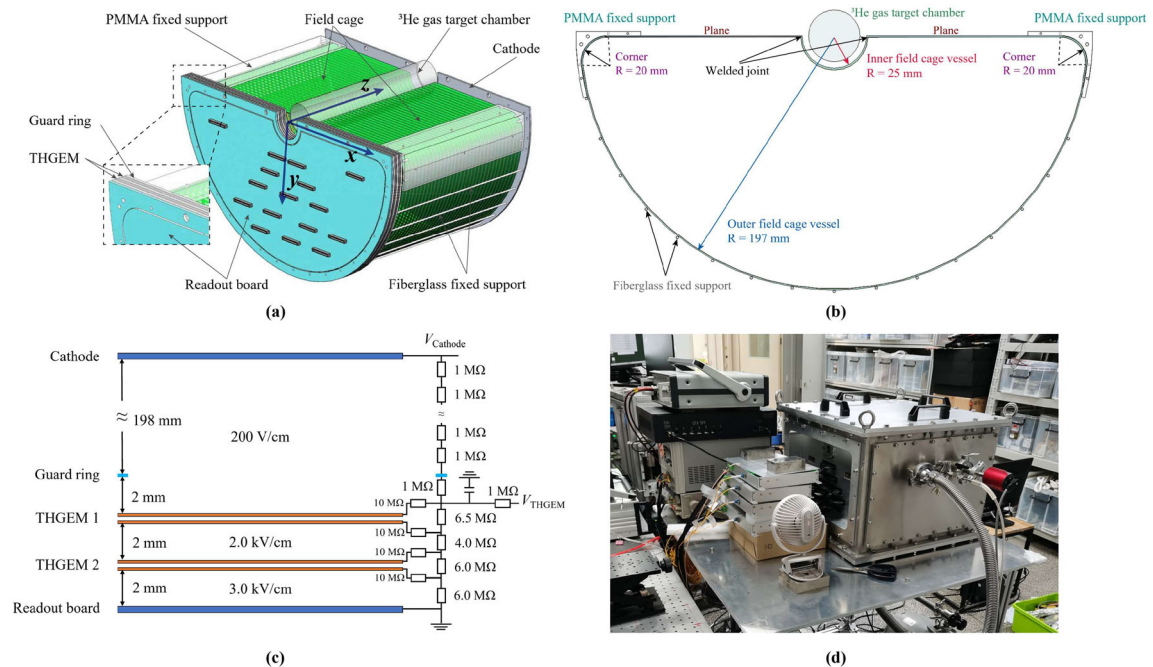

Fig. 4 Design schematic view of the scTPC structure (**a**). The shape and configuration of the field cage (**b**). Schematic view and HV distribution scheme for the scTPC detector module (**c**). The drift region is between the cathode and THGEM 1. The transfer region is between THGEM 1 and THGEM 2. The induction region is between THGEM 2 and the readout board. Physical view of the vacuum chamber (**d**)

The THGEM is composed of a double-sided copper-clad FR4 substrate that is perforated with densely spaced holes of 300 µm in diameter and 800 µm in pitch. The FR4 substrate has a thickness of 800 µm, while the copper is 17 µm thick. The active region of the THGEM is semicircular in shape, matching the geometry of the scTPC.

2.4 Field cage

The field cage of the scTPC is a semi-cylindrical structure, as illustrated in Fig. 4(b). The ion beam traverses through the center of the field cage along the axial direction and collides with the ^{3}He gas enclosed within the target chamber. To accommodate the ion beam and ^{3}He gas target chamber, the
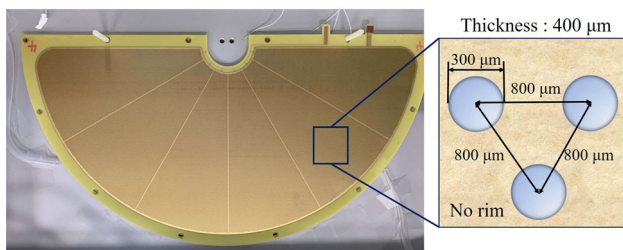
Fig. 5 Physical (right) and microscopic (left) view of the THGEM foil
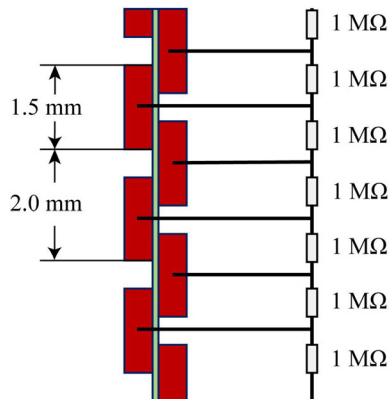
Fig. 6 Microstructure of the field cage. Our field cage is a 'mirror' electrode structure, where the size and pitch of the copper strips on the inner and outer surfaces are the same

inner field cage vessel adjacent to the ^{3}He gas target chamber has a small half-cylindrical shape with a 25 mm radius and is concentric with the larger outer semi-cylindrical field cage with a 197 mm radius. The length of the field cage is 200 mm. There is a groove left in the gasket between the THGEM and the field cage for gas exchange.

To achieve a homogeneous electric field inside the field cage, 1.5 mm wide and 2 mm pitch parallel copper strips are etched on both sides of the FR4 substrate [36,37]. The copper strips on opposite sides are half-pitch staggered as shown in Fig. 6. The neighboring strips are connected with 1 MΩ resistors, which provide a gradual potential decrease across the strip gap through voltage division of the resistor chain. We performed a simulation to estimate the three-dimensional electric field using COMSOL [38] to evaluate the electric field uniformity of the active area, as shown in Fig. 7. The inhomogeneity of the electric field can reach 0.5‰ at a distance of 10 mm from lowest edge of the inner field cage arc and 0.3‰ at a distance of 15 mm from lowest edge of the inner field cage arc.

Manufacturing and maintaining a highly homogeneous electric field in the special-shaped field cage is challenging, shown as Fig. 8(a). To address this issue, the printed circuit board (PCB) was chosen due to its flexibility in bending to curved surfaces. A 0.3 mm thick PCB was used as it offers

easy bending, sufficient mechanical strength, and is not easily breakable. The copper layer was kept as thin as possible at 10 μm to reduce resistance to the reaction products. The outer field cage vessel, two corners, and two planes are manufactured from a single PCB, shown as Fig. 8(b). The corner of the field cage was bent into a 20 mm radius curved face from a 3D-printed Polymethyl methacrylate (PMMA) fixed support and shaped with UV-curable adhesive, shown as Fig. 8(c). The semi-cylindrical outer field cage vessel was supported by 2 mm diameter fiberglass rods. Under the action of tension and with the support of fiberglass rods, the PCB will naturally form a complete semicircular surface. The inner field cage vessel is semi-cylindrical as well, shown as Fig. 8(d). A semi-cylindrical aluminum mold was used to fabricate the inner field cage vessel [39]. The PCB was shaped into a semi-cylindrical surface under pressure. On the upper plane of the field cage, the welding pads at the junction of the inner and outer field cage vessels were connected with solder. The dimensions of the inner field cage are the same as those of the outer field cage.

2.5 Readout board

The scTPC's readout board (see Fig. 9) is a 3 mm thick PCB with conductive pads on the upper surface. The total number of readout channels is 1014. The board is divided into two parts. The sector in the middle is the test zone, including 886 zigzag-shaped pads and the rest sector is the non-test zone including 128 square pads with 18 mm sides. The pads in the non-test zone are grounded. Readout electrodes with zigzag patterns have been used widely for improving position resolution and reducing the number of pads [40–43]. The zigzag-shaped pads utilized in the scTPC have a height of 7.29 mm and a width of 3.43 mm. The distance between two adjacent pads in the same row is 4 mm. The distance between two adjacent rows of pads is 7.5 mm. At the backside of the board, 14 connectors connected to the front-end electronics via customized data transmission cables are welded.

2.6 Readout electronics and data acquisition system

The readout electronics for the scTPC (see Fig. 10) is based on the ASIC for General Electronics for TPC (AGET) chips [44,45]. Several front-end cards (FECs) and one data collection module (DCM) are contained in this system. There are 64 channels for signals and 4 fixed pattern noise (FPN) channels in an AGET chip, and one FEC comprises 4 pieces of chips. Each channel is integrated with the charge sensitive amplifier (CSA), analogue filter, and switched capacitor array (SCA). The CSA has 4 adjustable gains, corresponding to 4 dynamic ranges of 120 fC, 240 fC, 1 pC, and 10 pC. The peaking time of the analogue filter can be selected from 50 ns to 1 μs. The SCA can continuously sample and memorize

Fig. 7 Electric field simulation: Three-dimensional view **(a)**, side view of *XY* plane **(b)**, and side view of *YZ* plane **(c)**
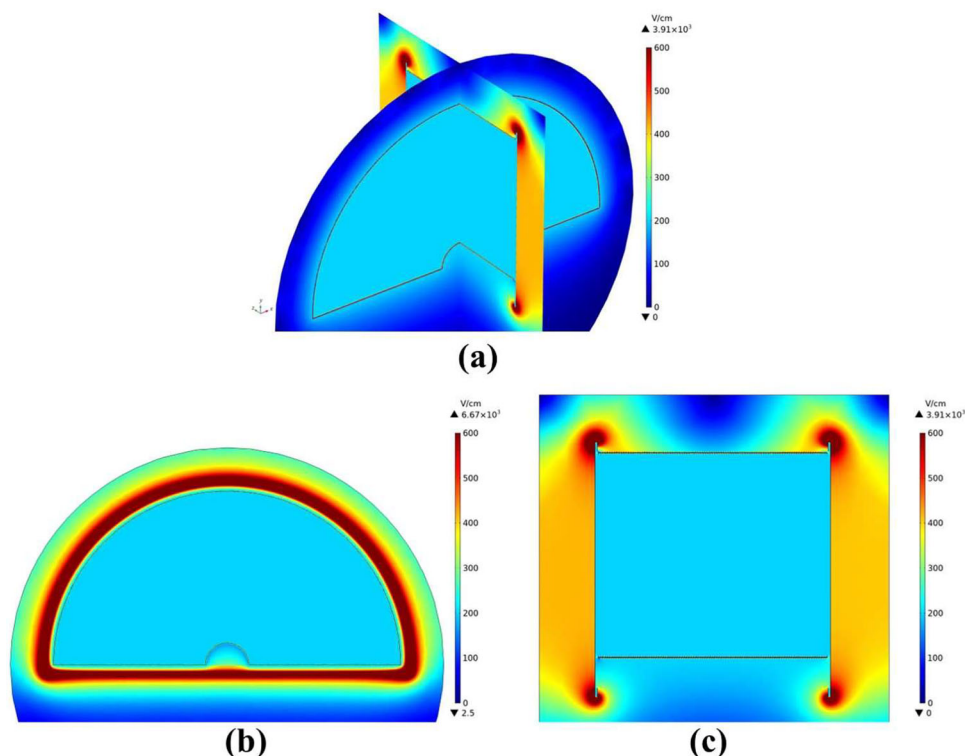
analogue signals, with 512 time buckets (namely 512 sample cells) and a selectable sampling frequency varying from 1 to 100 MHz. After being processed by the AGET chip, the signal is digitized by the 12-bit analog-to-digital converter (ADC) and packaged by a field programmable gate array (FPGA) chip. The two-way connection and communication between the DCM and FECs are set up with optical fibers. The DCM collects data from FECs and sends the control signal and global trigger to FECs. After gathering data from FECs, the DCM transmits the data to the computer via Ethernet. 4 pieces of FECs, installing 16 AGET chips and providing 1024 channels, are used in the experiment. The connector of the readout board to electronics is the Samtec ERM8-040-05.0-L-DV-TR 80-pin connector and ERM8-070-05.0-L-DV-TR 140-pin connector (see Fig. 10).

3 Performance test and data analysis

3.1 Optimal operational state for the scTPC

The operational state of the scTPC was determined using the 5.9 keV X-ray of a ^{55}Fe radioactive source. The operating voltages of the upper and lower THGEM foils are 650 V and 600 V, respectively. The electric fields in the drift region and induction region are 2 kV/(cm· atm) and 3 kV/(cm· atm), respectively. The operating gas is Ar (95%) + iC$_4$H$_{10}$ (5%) at local atmospheric pressure (850 mbar). The variation in the

effective gain and energy resolution (FWHM) of the two-layer THGEM foils was tested over a long term of continuous operation for a total of 120 h (see Fig. 11). Because the relative change in gain can characterize the THGEM's performance, the position of the full energy peak in the ^{55}Fe's X-ray energy spectrum, i.e., the "*Mean*" in Fig. 11(a), can serve as the relative effective gain. The energy resolution is equal to the ratio of the FWHM to the peak position of the full energy peak (*Sigma*· 2.36/*Mean*). The gain of the double-layer THGEM foils initially decreased with time, and stabilized after 24 h, shown as Fig. 11(b). The energy resolution exhibited no significant fluctuation throughout the period. Therefore, the data acquisition should be started after the scTPC has been powered for about 24 h when the gain of the THGEM has been stabilized.

3.2 Data analysis

The typical signals of α particles from ^{241}Am are shown as Fig. 12. The test is detailed in Sect. 3.4. The indexes of FPN channels are 11, 22, 45, 56 of each AGET if 68 channels are named from channel 0 to channel 67, which can be used to determine the noise level introduced by the electronics and the baseline shape to improve resolution [44]. For one trigger event, the average of 4 FPN channels is calculated and subtracted from the original signals. And then, the first 50 and last 200 time buckets of signals after the FPN correction, averaged and regarded as the overall baseline, are

Fig. 8 Physical view of field cage: The completed field cage (**a**), outer field cage vessel PCB (**b**), corner fixed support (**c**), and inner field cage vessel (**d**)

(a)

(b)

(c)

(d)
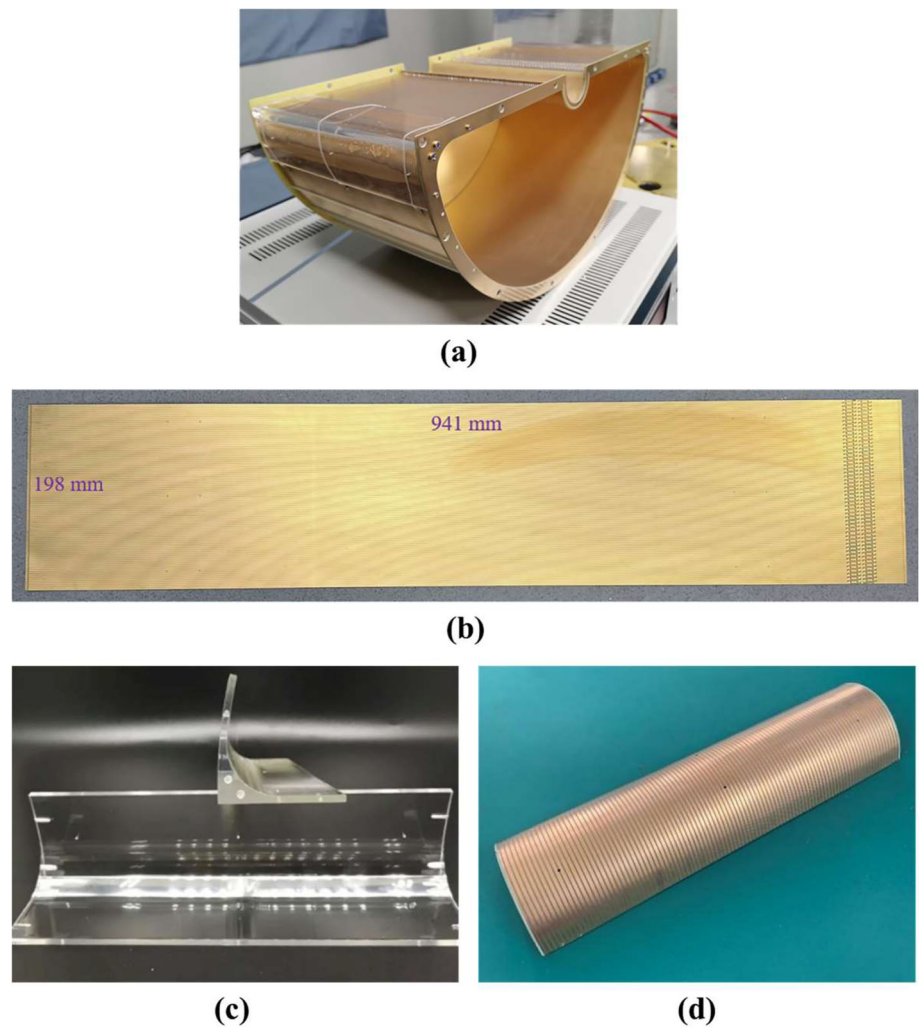
**Fig. 9** Layout diagram of the readout board
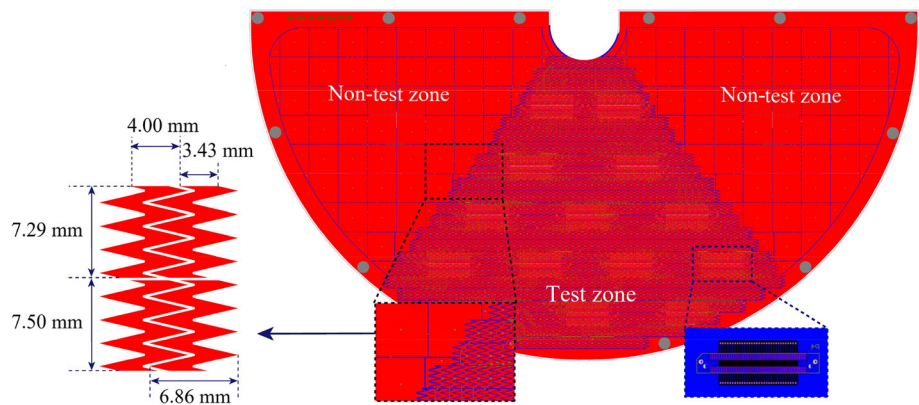
subtracted further to obtain the FPN-baseline corrected signals for the next steps in processing the data, e.g., waveform fitting, extracting amplitude, etc.

The output waveform from the AGET has an asymmetric shape, and therefore a special fitting function is constructed to fit the waveform to extract the information contained in the signal waveform. Generally, the *asymmetric generalized Gaussian distribution* (AGGD) [46] was used for fitting (see

Fig. 13) by constructing two asymmetric Gaussian functions to fit the rising edge and falling edge respectively, with the maximum value as the boundary. The *probability density function* of the AGGD is defined as:

$$f(x, \alpha, \beta_l, \beta_r) = \begin{cases} \frac{\alpha}{(\beta_l+\beta_r)\Gamma(\frac{1}{\alpha})} e^{-\left(\frac{-x+\mu}{\beta_l}\right)^\alpha} & \text{if } x < \mu \\ \frac{\alpha}{(\beta_l+\beta_r)\Gamma(\frac{1}{\alpha})} e^{-\left(\frac{-x+\mu}{\beta_r}\right)^\alpha} & \text{if } x > \mu \end{cases} \quad (1)$$

Fig. 10 Schematic view of
readout electronics for the
scTPC. In the red box are
connectors and data
transmission cables between the
readout board and electronics
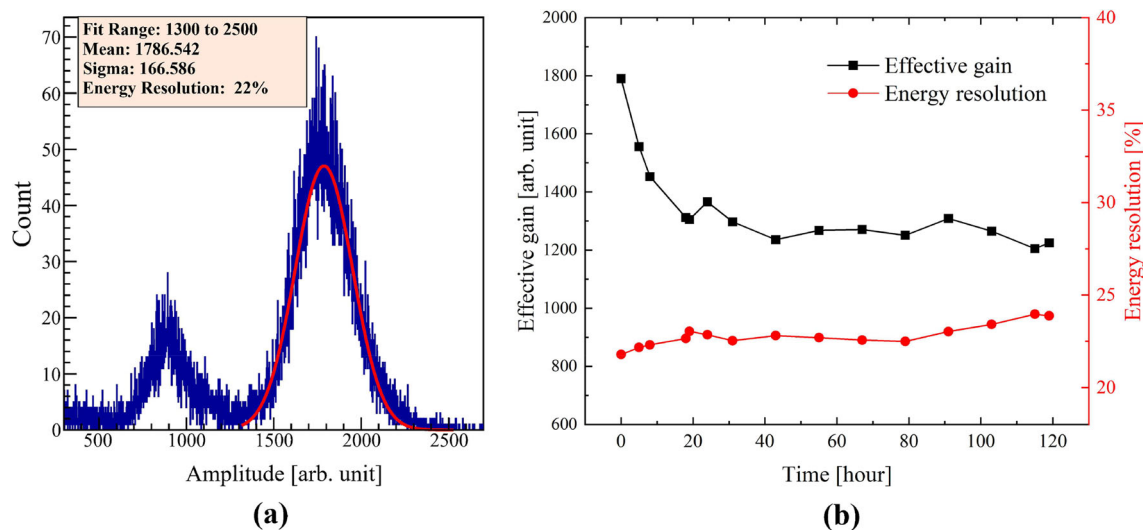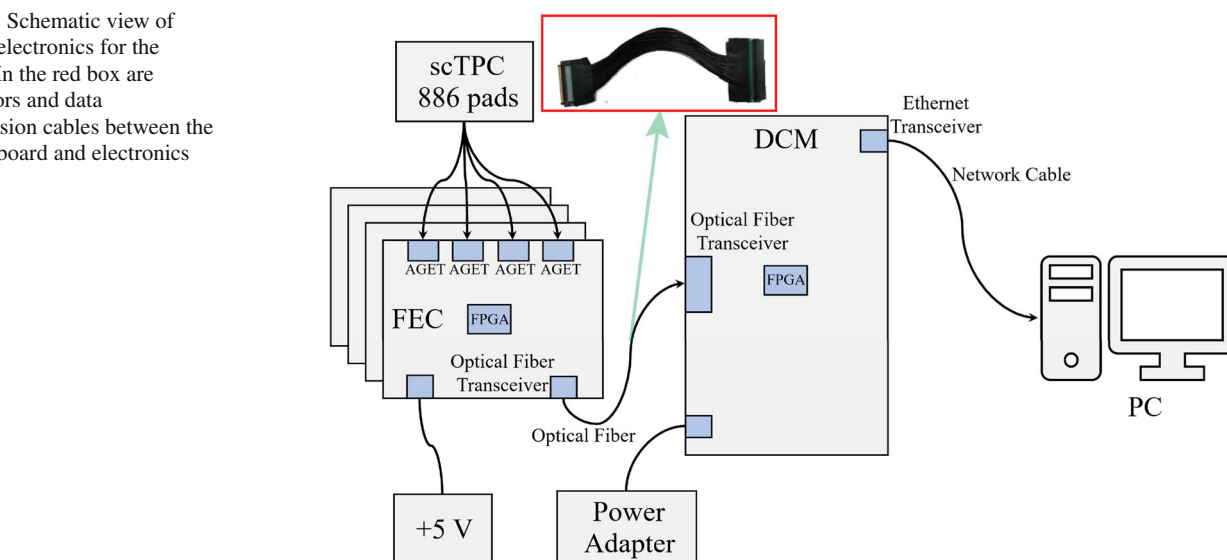
Fig. 11 Energy spectrum of the ^{55}Fe source at 0th hour **(a)** and curves of the effective gain and energy resolution of double-layer THGEM foils under long-time operation **(b)**. In figure **(a)**, the red line is the Gauss fitting curve

where the α (*AmpValue*) represents the waveform ampli-
tude, and the μ (*peakTime*) is the time corresponding to the
highest peak position. The β_l (*LeftBeta*) represents the ris-
ing time of the waveform defined as the time it takes for the
rising edge to go from 10% to 90% of its amplitude, and the
β_r (*RightBeta*) represents the falling time of the waveform
defined as the time it takes for the falling edge to go from
90% to 10% of its amplitude. Γ is the gamma function.

3.3 Drift velocity measurement using UV laser

The drift velocity of electrons in the TPC is the key to recon-
structing the three-dimensional track of the charged particle.
The 266 nm UV laser was used for drift velocity measure-
ment in the scTPC, which is a common method [17,47,48].

The laser is generated by the Q-SMART 450 [49], which
is capable of delivering laser beam with a maximum power
of 45 mJ. The laser beam power is reduced with the beam
splitters and attenuators so that the signal generated by the
laser beam can be acquired by the AGET system, where the
power is about 4 μJ. The laser beam in the vacuum cham-
ber was split into two beams using a semi-transmissive mir-
ror (50% transmission and 50% reflection). These two laser
beams would enter the gas volume of the scTPC through two
collimator holes (diameter about 1 mm) on the inner wall of
the field cage, shown as Fig. 14, parallel to the readout plane.
According to the position of the collimator holes in the inner
field cage, corresponding holes were left in the outer field
cage, and two Si-photodiodes (Si-PDs) were placed outside
the holes in the outer field cage. Two lasers were observed to

(a)

(b)
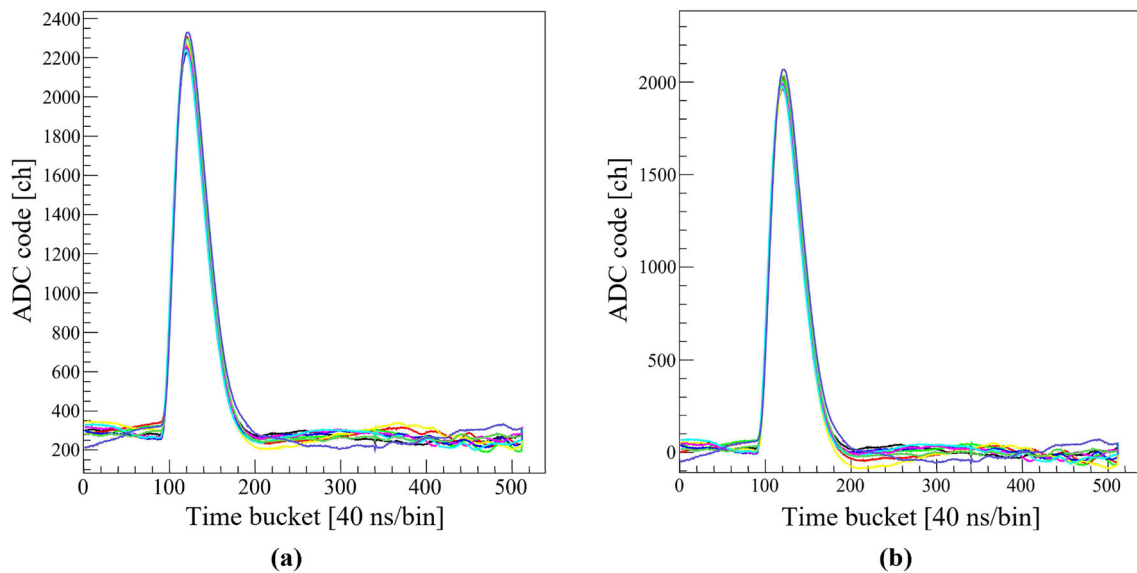
Fig. 12 The typical waves for the signals of α particles from ^{241}Am radioactive source. **a** Shows the original signals and **b** shows the signals corrected by the FPN channels and baselines. Different colors represent waves of different channels. The sampling frequency and gain of AGET is 25 MHz and 240 fC, respectively


AmpValue:	1496.485
LeftBeta:	13.811
RightBeta:	35.052
peakTime:	115.162
χ^2/ndf:	843.719
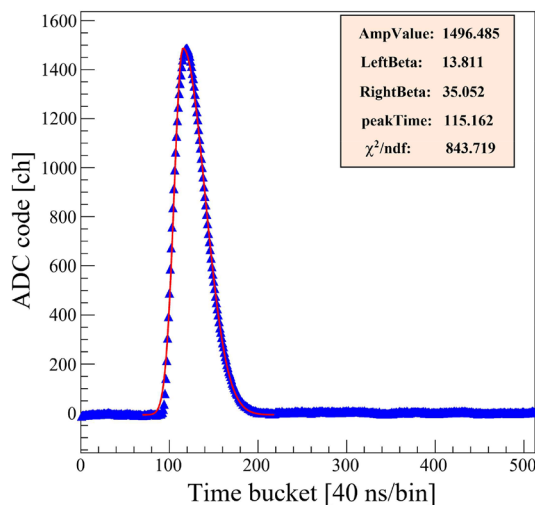
Fig. 13 AGGD fitting of the waveform. The sampling frequency and gain of AGET is 25 MHz and 240 fC, respectively

be aligned with the collimator holes of the inner field cage and the two Si-PDs had signals at the same time, then it meant that the two laser beams were parallel. The holes A, B and C drilled during the manufacturing process of the field cage are shown in the Fig. 14(c), with hole A 2 cm from the THGEM. The distance between adjacent holes is 8 cm. The distance between two collimator holes (holes B and C) in the test is 8 cm.

The long track of the laser is shown in Fig. 15. In the x–y plane, there is no obvious bending, indicating a uniform electric field in the middle part of the scTPC. When the pro-

jections in the x–y plane of the two laser beams overlap, shown as Fig. 15, the two laser beams have different electron drift times in the z direction (i.e., the electron drift direction) due to the different distances from the readout board. The difference in distance (8 cm) results in a time difference of about 2 μs (50 bins). The sampling window width is $512 \cdot 40$ ns $= 20.48$ μs, and the 2 μs time difference allows the signals of two laser beams display together in one sampling window resulting in the double-peak waveform in Fig. 16. The difference between the two peaks is the difference between the electron drift times produced by the two laser beams. The right peak position corresponds to the track further away from the readout board and the left peak corresponds to the track closer to the readout board. The drift time difference between two lasers' tracks can be exploited to calculate the drift velocity of the ionized electron under a certain electric field and operating gas in the drift region. Figure 17 shows the drift time difference when the electric field is 200 V/(cm· atm) in Ar (95%) + iC$_4$H$_{10}$ (5%). We measured and simulated the electron drift velocity under several drift electric fields in Ar (95%) + iC$_4$H$_{10}$ (5%), as shown in Fig. 18. The tests were all performed at local atmospheric pressure (850 mbar), and then the electric field was converted to reduced field strength. When the electric field is 200 V/(cm· atm), the deduced drift speed is 4.19 ± 0.29 cm/μs from the experiment from Fig. 16. This result is in good agreement with the calculated value of 4.11 cm/μs based on the MediumMagboltz of Garfield++ [50], which provides an interface to the Magboltz program [51]. It should be noted that the existence of the double-peak waveform makes the peak positions from

(a)

(b)

(c)
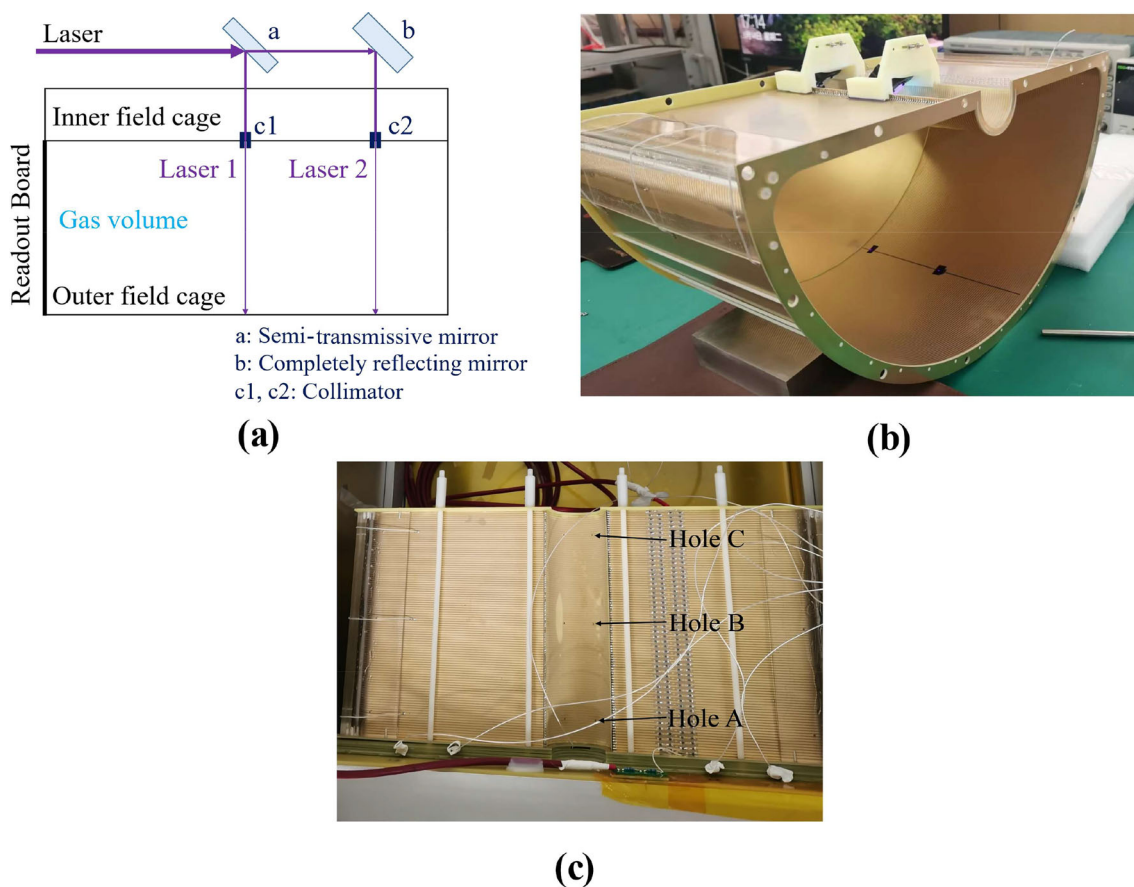
Fig. 14 Laser mapping system. Figure **(a)** is the schematic of the laser light path. Figure **(b)** is the physical view of the mirror holders and field cage. Figure **(b)** is not the assembly during the test because the scTPC was placed in the chamber during the test. The two white holders, i.e., the mirror holder, are made by 3D printing and the material is resin, which can avoid interference with the electric field. Figure **(c)** shows holes A, B and C drilled during the manufacturing process of the field cage

the fitting deviate, which we consider to be the main source for the uncertainty of the drift velocity. As the electric field increases, the time difference between two laser beams is smaller, and two peak positions are gradually closer to each other, leading to an increase in the probability of deviation in the fitting, which is reflected in the error of the drift velocity. Increasing the distance between the collimator holes is a good way to increase the separation between the two peaks and thus avoid influencing each other. But there is not enough space to place a mirror holder at hole A. In fact, in our future beam experiments, the probability that projections of two tracks in the $x-y$ plane overlap is very low, so the uncertainty of the time extraction described above will be reduced. In addition, due to the width of the laser beam (i.e., the 1 mm diameter of the collimator holes), the laser's track is not suitable for measuring position resolution in this work.
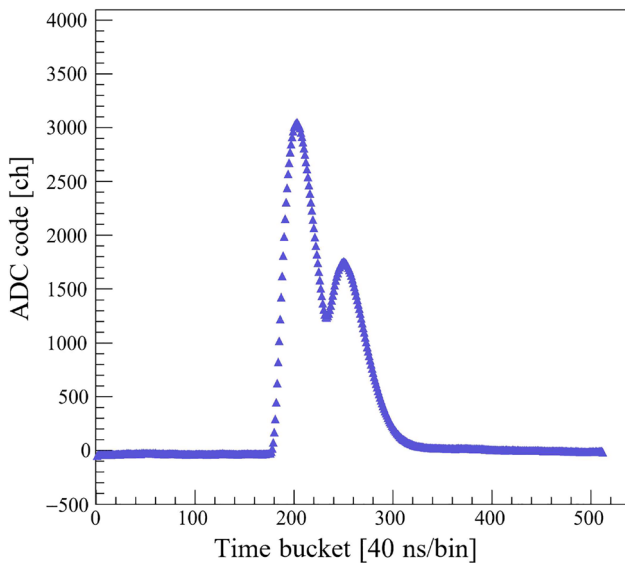
3.4 Performance test utilizing ^{241}Am α radioactive source

To measure the ability of the scTPC to detect charged particles, we tested the performance utilizing the 5.486 MeV α particle of ^{241}Am radioactive source. The radioactive source is attached to the outer side of the inner field cage vessel, facing the 1 mm diameter pinhole acting as a collimator in the inner field cage vessel, shown as Fig. 19(a). The field cage is capable of completely shielding 5 MeV α particles. The gas pressure was set to 850 mbar (local atmospheric pressure), and the particle could deposit completely in the scTPC, and create a short track (see Figs. 19, 20). The color of the pad represents the different charge deposition. All fired pads in each row are regarded as a cluster. The weighted charge center coordinate of the cluster, $(x_{n,c.c.}, y_{n,c.c.})$, in the nth row is

$$\begin{cases} x_{n,c.c.} = \frac{\sum_i x_{n,i} Amp_{n,i}}{\sum_i Amp_{n,i}} \\ y_{n,c.c.} = y_{n,i} \end{cases}, \tag{2}$$
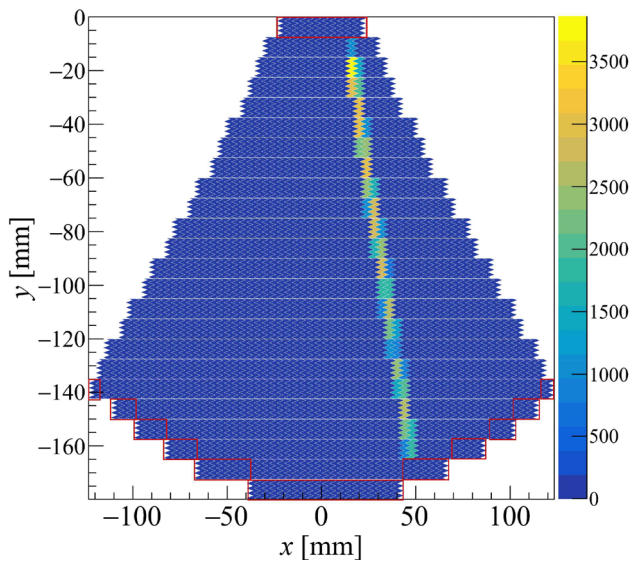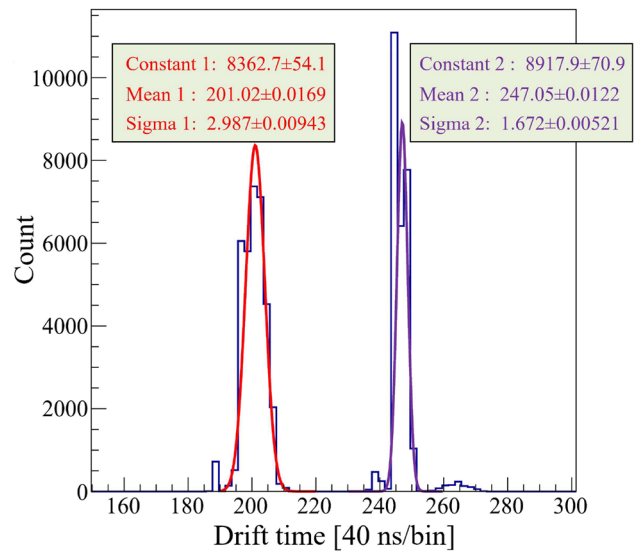
Fig. 15 Projection of a laser's track on the readout plate. The pads (in the red box) close to the field cage were ignored due to electric field distortion, about 69 pads (about 8% of the total). This rejection has little effect on the CE experiments because of the presence of a non-sensitive region outside the scTPC sensitive region
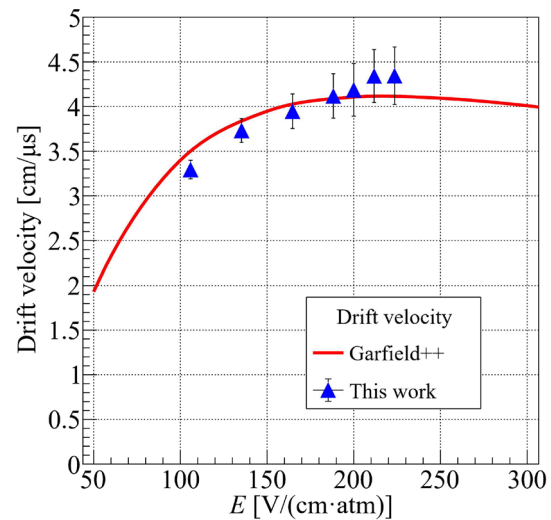

Fig. 17 Drift time distribution of two lasers' tracks at 200 V/(cm· atm)

Fig. 16 Double-peak signal generated by the laser. The sampling frequency and gain of AGET is 25 MHz and 240 fC, respectively

Fig. 18 Electron drift velocity measured in Ar (95%) + iC_4H_{10} (5%). The red line is the result of the Garfield++ simulation and the blue triangle is the experimentally measured value

where $(x_{n,i}, y_{n,i})$ and $Amp_{n,i}$ are the center position and charge deposition of the fired pad in the nth row and ith column, respectively. In the y direction, the geometric center of the readout pad is adopted as the charge center of the cluster. Thus, a series of clusters' coordinates are obtained, and the projected α particle track can be reconstructed by fitting the positions of clusters on the x–y plane with a linear function, shown as Fig. 20(a) It can be seen from Fig. 20 that

the charge deposition increases significantly at the end of the range, showing a clear Bragg peak distribution.

The signal led from the lower surface of the THGEM 2 is amplified, discriminated and converted into a TTL signal, which is then used as an external trigger for the AGET. By accumulating amplitudes of all signals under one track and then counting all effective tracks, the energy spectrum of the α particle can be obtained. The angle of the reconstructed track with the x-axis is defined as φ. Note that, effective events are limited to incident events within $\pm 1.5°$ of the collimator direction, $\varphi = 69.5° \sim 72.5°$. The energy spectrum is shown in Fig. 21, with an energy resolution (FWHM) of 5.6%. In fact, the energy resolution of the α particle could
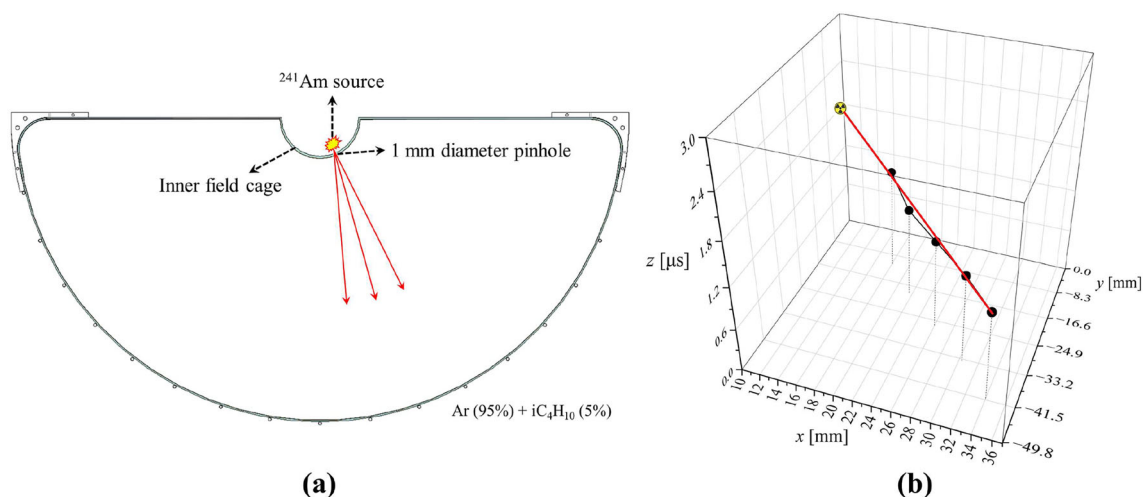
Fig. 19 Schematic diagram of the α test (**a**) and the three-dimensional view of a typical α track (**b**). The black point is the charge center of the cluster in the $x-y$ plane and the red line is to lead the eye instead of the real α track in (**b**)
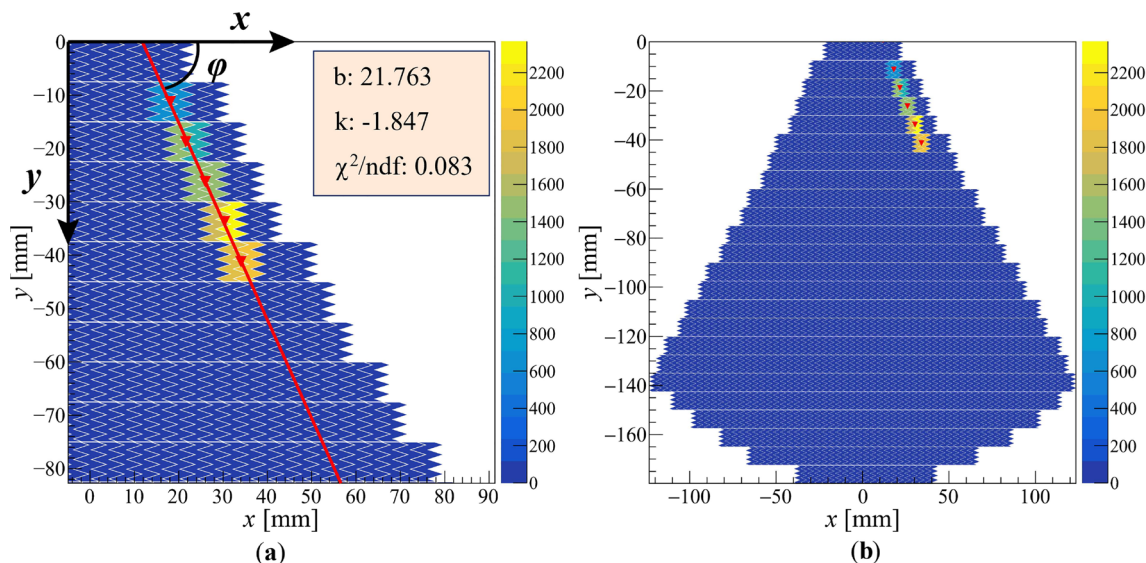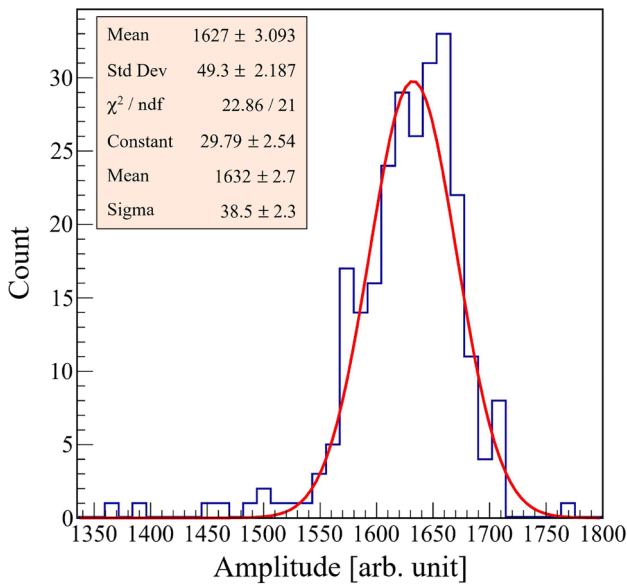

Fig. 20 Projection of an α particle's track on the readout plate. The red triangle marker is the charge center for each cluster, and the red line is the fitted line. The distance from the red triangle to the red line is the *residual* of a cluster

be further improved, since the source was placed on the outside of the field cage and some of the energy was lost in the non-sensitive region of the gas.
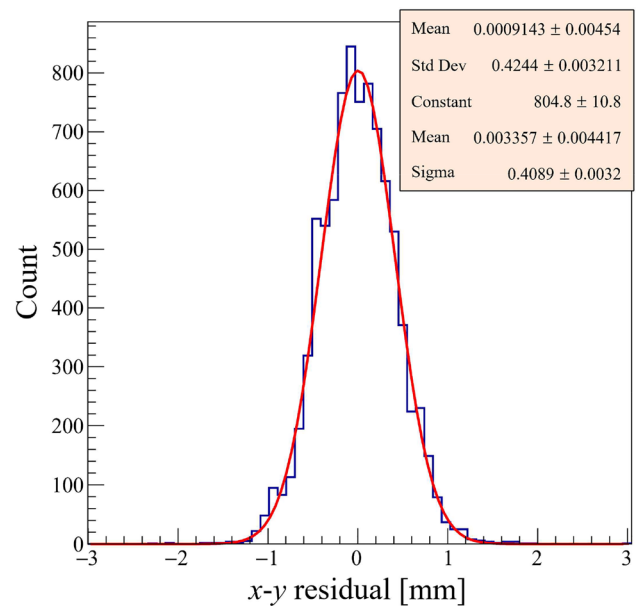
The track resolution has little relation to the energy, so the chosen azimuthal angle range can be larger ($\varphi = 65° \sim 90°$). The position resolution is the *residual* obtained from the linear fitting of the α particle track on the $x-y$ plane [52,53]. The distance from the cluster center position to the fitted line was defined as the $x-y$ direction *residual*, and its standard deviation was equivalent to the $x-y$ resolution. For all clusters for a number of effective tracks, the *residual* distribution is fitted by Gaussian, and the *Sigma* is the resolution. The position resolution in the $x-y$ plane of the scTPC was 409 μm (shown in Fig. 22). The response of the pad to charged

particles depends on the azimuthal angle φ. The position resolution is expected to be proportional to $\tan(|90° - \varphi|)$ [52]. For the readout electrode in the scTPC, $|90° - \varphi|$ varies from approximately 0° to 35°, resulting in a slight degradation in position resolution. However, for the position resolution extraction, we considered $\varphi = 65° \sim 90°$, an average value across various azimuthal angles. This choice yielded a satisfactory position resolution, indicating a limited impact of the azimuthal angle on position resolution.

In the z direction, $x-y$ coordinate values were converted to the distance r from the vertex (first cluster's center) of the two-dimensional track. The z-directional drift distance is represented by the rising time of the signal waveform (i.e., *LeftBeta* in Fig. 13). Similar to the $x-y$ direction, the z posi-
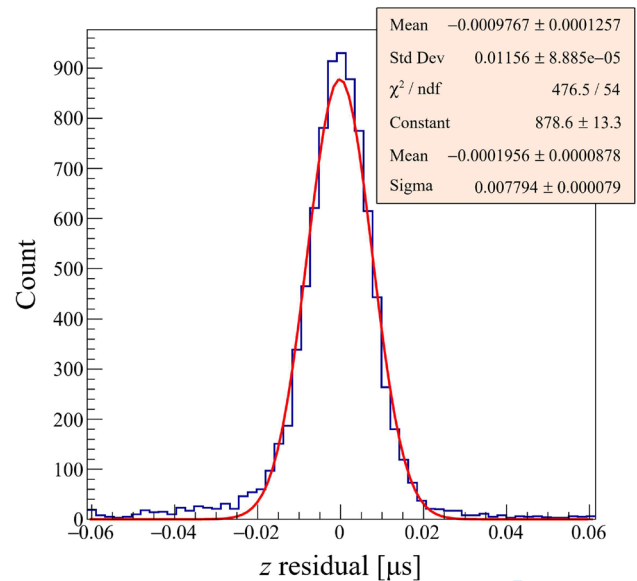
Mean	1627 ± 3.093
Std Dev	49.3 ± 2.187
χ^2 / ndf	22.86 / 21
Constant	29.79 ± 2.54
Mean	1632 ± 2.7
Sigma	38.5 ± 2.3

Fig. 21 Energy spectrum of ^{241}Am source acquired by the scTPC. The energy resolution ($\eta = 2.36 \cdot$ *Sigma* /*Mean*) is given as 5.6% by using a Gaussian fit to the energy spectrum

Mean	0.0009143 ± 0.00454
Std Dev	0.4244 ± 0.003211
Constant	804.8 ± 10.8
Mean	0.003357 ± 0.004417
Sigma	0.4089 ± 0.0032

Fig. 22 *Residual* distribution of linear fitting of track in the x–y plane. Fitting with Gaussian, the position resolution (*Sigma*) in the x–y plane is obtained as 409 μm

tion resolution was deduced based on the linear fitting of the α particle tracks on the r-z plane. The distance from the reconstructed cluster position to the fitted line was defined as the r–z direction *residual*, and its standard deviation was equivalent to the z resolution (shown in Fig. 23). The z time resolution was 7.79×10^{-3} μs. Based on the electron drift velocity of 4.19 cm/μs measured in the previous section, the z position resolution of the scTPC is approximately 326 μm. Considering a 5 cm long α particle track, a position resolution of 326 mm corresponds to an angular resolution of about 0.4°. These energy and position resolutions provide better conditions for the next step of experimental data analysis and processing.

While the *residual* method is commonly used to assess the spatial resolution of gaseous detectors, it may not fully consider systematic errors arising from factors like the absolute positioning of readout pads and electric field distortions. Since the *residual* analysis is a relative measurement, some errors may offset each other; e.g., electric field distortions can cause an overall shift of the track, which may not be reflected in the *residual*. As a result, some effects that are significant in absolute measurements may be neglected in relative measurements. Therefore, we refined our position resolution extraction process by excluding edge pads (see Fig. 15) and selecting tracks within regions characterized by uniform electric fields. The *residual* can reflect the reconstructed track's accuracy to some extent by minimizing systematic errors. In addition, the vertex of the track was tried to be reconstructed to measure the positioning accuracy of the scTPC from another perspective. Based on the linear fit


Mean	−0.0009767 ± 0.0001257
Std Dev	0.01156 ± 8.885e−05
χ^2 / ndf	476.5 / 54
Constant	878.6 ± 13.3
Mean	−0.0001956 ± 0.0000878
Sigma	0.007794 ± 0.000079

Fig. 23 *Residual* distribution obtained by linear fitting of track projected in the z direction. Fitting with Gaussian, the time resolution (*Sigma*) in the z direction is 7.79×10^{-3} μs

to the serial cluster coordinates of the track in the x–y plane, the vertex coordinate (*Vertex_x*, *Vertex_y*) can be obtained by extrapolating along the line to the pinhole. The actual collimated hole location is approximately (12.8, −4.1) (in mm) on the curved surface of the inner field cage. The vertex derived from the track is (13.0, −3.8) (in mm), as shown in Figs. 24 and 25, which is closely matches the actual vertex. Using the width $\sigma_{x(y)}$ (with width referring to the standard
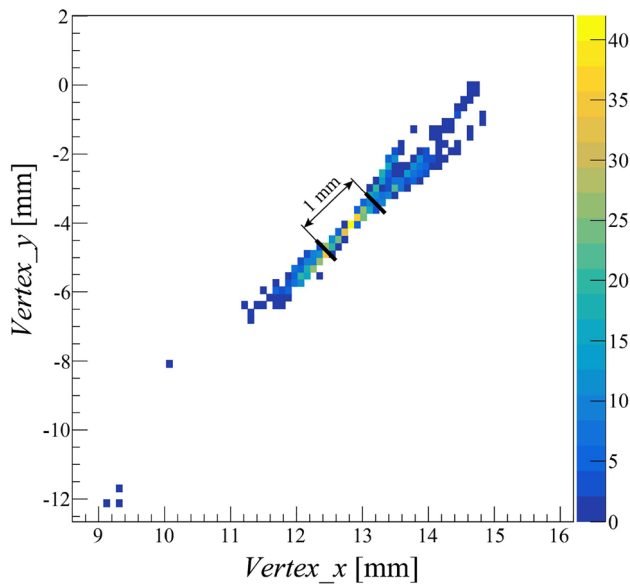
Fig. 24 Distribution of the reconstructed vertex coordinate in the $x-y$ direction from the track of the α particle. The black lines represent the edges of the pinhole

deviation throughout the paper) of the reconstructed vertex in the x and y directions (see Fig. 25), the positioning accuracy of the vertex is obtained as $\sigma = (\sigma_x^2 + \sigma_y^2)^{1/2} = 1.6$ mm, including the width of the 1 mm pinhole.
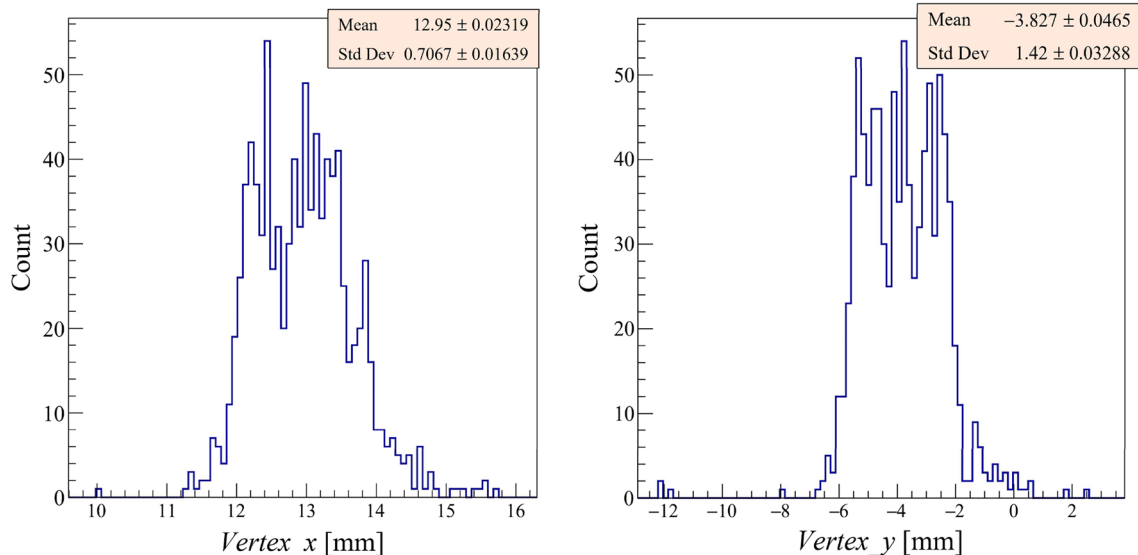
4 Simulation of beam experiment

In order to simulate the operation of the detector in a beam experiment of ^{17}C $(^3$He,$t)^{17}$N CE reaction, we set up a model according to the experimental setup in Geant4, the same as the model in Sect. 2.1 and shown in Fig. 26. The non-elastic scattering process was simulated using the FTFP_BERT_ATL physics list of Geant4 [54]. According to the reconstructed kinematic plot for ^{17}C$(^3$He,$t)^{17}$N CE reaction (see Fig. 27), it can be seen that various charged particles can be clearly distinguished within the ejection angle of 76° $\sim$ 85°. The simulation results show that the most productive product is the proton, whereas the product of the elastic scattering, ^{3}He, is quite small. Therefore, we believe that ^{3}He is highly likely to be decomposed by a heavy ion beam of 500 MeV/nucleon, leading to the dominance of proton and deuteron counts. Although the yield of the CE reaction is relatively smaller compared to other scattering processes, especially protons, it is still measurable and can be discriminated. The rationality of our concept and the setup of the detector is validated.

A further estimation of the cross section and count rate for ^{17}C$(^3$He,$t)^{17}$N was performed based on cross section data from a similar CE reaction experiment, ^{13}C$(^3$He,$t)^{13}$N with the ^{3}He energy of 450 MeV [1]. Considering the major reaction channels (ground state and 3.502 MeV excited state), the total cross section for a 4π sr solid angle is about 0.48 mb calculated from the differential cross section versus the scattering angle in the center-of-mass system. If the gas pressure

Fig. 25 Distributions of the track vertices in the x (**a**) and y (**b**) directions. The vertex coordinate, determined using *Mean*, is (13.0, -3.8) (in mm) with widths (standard deviation) of 0.71 mm and 1.42 mm in the x and y directions, respectively. Because the center coordinate of
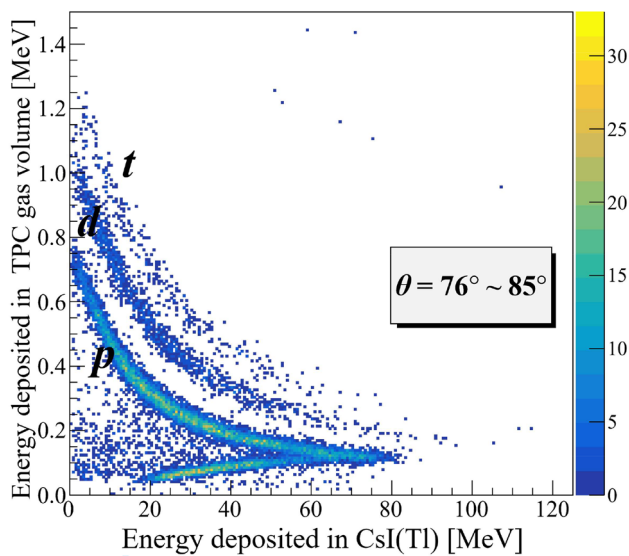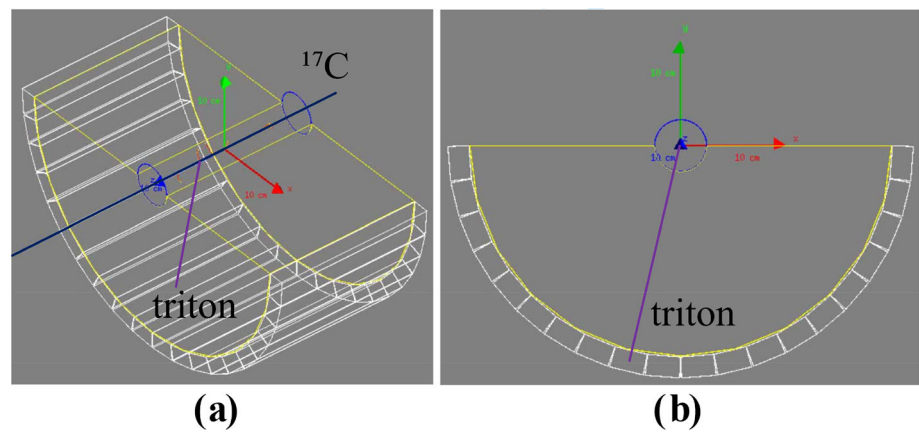
the cluster in the y-direction is adopted from the geometric center of the pad, the positioning accuracy in the y-direction is worse than that in the x-direction

Fig. 26 Simulated ^{17}C(^{3}He,t)^{17}N CE reaction at a beam energy of 500 MeV/nucleon and ^{3}He gas target at 3 atmospheres. Three-dimensional view of the track (**a**) and its projection on the readout pad plane (**b**). The blue line represents the track of ^{17}C and the purple line represents the track of the triton

Fig. 27 Simulated $\Delta E - E$ distribution of products from the bombardment of the ^{3}He target by the 500 MeV/nucleon ^{17}C beam

tive of spin-isospin excitation widely. Traditionally, experiments have been carried out using ^{3}He or triton beam from accelerators to study a series of CE reactions involving stable nuclei via (^{3}He,t) or (t,^{3}He). We propose to exploit the radioactive isotope beam of HIRFL to perform (^{3}He,t) CE reactions in inverse kinematics, which can extract the characteristics of neutron-rich or neutron-drip-line nuclei.

Consequently, we are constructing a ΔE-E detection system to detect (^{3}He,t) CE reactions in inverse kinematics, with the scTPC playing a crucial role in measuring ΔE and reconstructing particle tracks. This paper focuses on the design, construction, performance testing, and data processing of the scTPC prototype.

The scTPC is semi-cylindrical with a length of 20 cm and a radius of around 20 cm, based on THGEM technology using 886 zigzag-shaped pads. In order to provide a uniform electric field, a semi-cylindrical field cage was specially designed and manufactured. The scTPC prototype was operated in the Ar/iC$_4$H$_{10}$ (95/5) gas mixture and the AGET is utilized as readout electronics.

The basic performance of the scTPC was tested using the laser and ^{241}Am radioactive source. When the electric field is 200 V/(cm· atm), the deduced electron drift velocity is 4.19 $\pm$ 0.29 cm/μs from the experiment. This result is in good agreement with the calculated value of 4.11 cm/μs based on Garfield++. The energy resolution for 5.486 MeV α particles is 5.6%. The spatial resolutions on the pad plane and along the drift direction are measured at 409 μm and 326 μm, respectively. The z position resolution determines the precision of angle measurement for the ejected t, where different angles correspond to different energies and reaction channels. The position resolution of 326 μm corresponds to an angular resolution of about 0.4°. Therefore, this z position resolution is of great significance. The vertex reconstructed from the track is in conformity with the actual vertex position. The energy and position resolutions (especially in the z-direction) provide better conditions for the next step of experimental data analysis and processing.

of the ^{3}He target is 3 atm, the target length is 20 cm, and the beam intensity is 10^6 pps (particles per second), the count rate is calculated to be about 1 pps. If only the kinematical range of our interest is taken into account, the scattering angle in the center-of-mass system $\theta_{c.m.} = 7.5° \sim 17°$, the circumferential angle φ covers about 70°, and the total cross section and count rate are about 0.01 mb and 0.02 pps. This calculation, although not including cross sections for all reaction channels of the ^{13}C(^{3}He,t)^{13}N CE reaction, not even the cross section of ^{17}C(^{3}He,t)^{17}N, gives a rough estimate of the cross section and count rate for the ^{17}C(^{3}He,t)^{17}N reaction at the order-of-magnitude level. This estimation provides us with a reference for the time duration of the beam experiments.

5 Summary and outlook

Charge exchange reactions at intermediate energies have been applied to study the structure of nuclei from the perspec-

The construction of the prototype detector is almost complete, and the experimental measurement of CE reactions will be carried out at the accelerator. With the $\Delta E - E$ telescope, we can select the ejected triton and calculate their differential reaction cross sections at different angles and energies, thereby exploring the internal structure of the atomic nucleus. At the same time, theoretical research on CE reactions in inverse kinematics is also underway. The success of the prototype experiment will lay the foundation for the polarized ^{3}He CE reaction experiment and the large-scale CE reaction detector.

Data Availability Statement This manuscript has no associated data or the data will be deposited. [Authors' comment: as for the data availability, the only data relevant to the publication is present in form of published graphs or tables. All the datasets and figures in the paper can be available from the corresponding authors upon request].

References

1. H. Fujimura et al., Nuclear structure of the spin-isospin excited states in ^{13}N studied via the (^{3}He, t) and (^{3}He, tp) reactions at 450 MeV. Phys. Rev. C **69**, 064327 (2004). https://doi.org/10.1103/PhysRevC.69.064327

2. R.G.T. Zegers et al., The (t,^{3}He) and (^{3}He,t) reactions as probes of Gamow–Teller strength. Phys. Rev. C **74**(2), 024309 (2006). https://doi.org/10.1103/PhysRevC.74.024309

3. R.G.T. Zegers et al., Extraction of weak transition strengths via the (^{3}He,t) reaction at 420 MeV. Phys. Rev. Lett. **99**(20), 202501 (2007). https://doi.org/10.1103/PhysRevLett.99.202501

4. B.M. Loc et al., Charge-exchange scattering to the isobaric analog state at medium energies as a probe of the neutron skin. Phys. Rev. C **89**(2), 024317 (2014). https://doi.org/10.1103/PhysRevC.89.024317

5. S.L. Tabor et al., The (^{3}He,t) reaction at 197 MeV on ^{12}C, ^{24}Mg, ^{28}Si and ^{40}Ca. Nucl. Phys. A **422**(1), 12–44 (1984). https://doi.org/10.1016/0375-9474(84)90429-9

6. E.-W. Grewe et al., (^{3}He,t) reaction on the double β decay nucleus ^{48}Ca and the importance of nuclear matrix elements. Phys. Rev. C **76**(5), 054307 (2007). https://doi.org/10.1103/PhysRevC.76.054307

7. H. Fujita et al., High resolution study of isovector negative parity states in the ^{16}O (^{3}He,t)^{16}F reaction at 140 MeV/nucleon. Phys. Rev. C **79**(2), 024314 (2009). https://doi.org/10.1103/PhysRevC.79.024314

8. P. Puppe et al., High-resolution (^{3}He,t) reaction on the double-β decaying nucleus ^{136}Xe. Phys. Rev. C **84**(5), 051305(R) (2011). https://doi.org/10.1103/PhysRevC.84.051305

9. J.H. Thies et al., The reaction on ^{76}Ge, and double-β-decay matrix element. Phys. Rev. C **86**, 014304 (2012). https://doi.org/10.1103/PhysRevC.86.014304

10. P. Puppe et al., High resolution (^{3}He,t) experiment on the double-β decaying nuclei ^{128}Te and ^{130}Te. Phys. Rev. C **86**, 044603 (2012). https://doi.org/10.1103/PhysRevC.86.044603

11. S. Giraud et al., Simulations and analysis tools for charge-exchange (d,^{2}He) reactions in inverse kinematics with the AT-TPC. Nucl. Instrum. Methods Phys. A **1051**, 168213 (2023). https://doi.org/10.1016/j.nima.2023.168213

12. S. Giraud et al., β^+ Gamow–Teller strengths from unstable ^{14}O via the (d,^{2}He) reaction in inverse kinematics. Phys. Rev. Lett. (2023). arXiv:2210.15866

13. L.J. Mao et al., Introduction of the Heavy Ion Research Facility in Lanzhou (HIRFL). J. Instrum. **15**, T12015 (2020). https://doi.org/10.1088/1748-0221/15/12/T12015

14. Y. Zhang et al., Density measurement through elastic electron scattering with a gaseous target at the Jefferson Lab. Chin. Phys. C **36**, 610 (2012). https://doi.org/10.1088/1674-1137/36/7/008

15. F. Sauli, Gaseous Radiation Detectors: Fundamentals and Applications (Cambridge University Press, Cambridge, 2014), pp. 292–326. https://doi.org/10.1017/CBO9781107337701

16. H.J. Hilke, Time projection chambers. Rep. Prog. Phys. **73**, 116201 (2010). https://doi.org/10.1088/0034-4885/73/11/116201

17. Z.C. Zhang et al., Studying the heavy-ion fusion reactions at stellar energies using time projection chamber. Nucl. Instrum. Methods Phys. A **1016**, 165740 (2021). https://doi.org/10.1016/j.nima.2021.165740

18. S.H. Kim et al., Development of a GEM-based time projection chamber prototype for low-energy rare-isotope beam experiments. Nucl. Instrum. Methods Phys. A **962**, 163687 (2020). https://doi.org/10.1016/j.nima.2020.163687

19. E. Koshchiy et al., Texas Active Target (TexAT) detector for experiments with rare isotope beams. Nucl. Instrum. Methods Phys. A **957**, 163398 (2020). https://doi.org/10.1016/j.nima.2020.163398

20. T. Ahn et al., The Notre-Dame Cube: an active-target time-projection chamber for radioactive beam experiments and detector development. Nucl. Instrum. Methods Phys. A **1025**, 166180 (2022). https://doi.org/10.1016/j.nima.2021.166180

21. Z.X. He et al., An optimization method of position resolution for gaseous thermal neutron detection based on time information. J. Instrum. **16**, P08020 (2021). https://doi.org/10.1088/1748-0221/16/08/P08020

22. S. He et al., Working properties of GEM-TPC at low pressure. JANDT **4**, 121–128 (2022). https://doi.org/10.1016/j.jandt.2022.09.002

23. A. Breskin et al., A concise review on THGEM detectors. Nucl. Instrum. Methods Phys. A **598**, 107 (2009). https://doi.org/10.1016/j.nima.2008.08.062

24. A. Breskin et al., The THGEM: a thick robust gaseous electron multiplier for radiation detectors. Nucl. Instrum. Methods Phys. A **623**, 132 (2010). https://doi.org/10.1016/j.nima.2010.02.172

25. W.Q. Yan et al., Performance study of a novel sampling TPC prototype detector based on THGEM. Radiat. Detect. Technol. Methods **3**, 23 (2019). https://doi.org/10.1007/s41605-019-0102-6

26. A. Bondar et al., Low-pressure TPC with THGEM readout for ion identification in accelerator mass spectrometry. Nucl. Instrum. Methods Phys. A **958**, 162780 (2020). https://doi.org/10.1016/j.nima.2019.162780

27. Z.M. Hu et al., Investigation on the performance of a thick ceramic gas electron multiplier. Nucl. Instrum. Methods Phys. A **1034**, 166824 (2022). https://doi.org/10.1016/j.nima.2022.166824

28. G.R. Satchler et al., Optical-model analysis of "quasielastic" (p, n) reactions. Phys. Rev. **136**, B637 (1964). https://doi.org/10.1103/PhysRev.136.B637

29. D.T. Khoa et al., Folding model study of the charge-exchange scattering to the isobaric analog state and implication for the nuclear symmetry energy. Eur. Phys. J. A **50**, 34 (2014). https://doi.org/10.1140/epja/i2014-14034-9

30. O.B. Tarasov, D. Bazin, LISE++: radioactive beam production with in-flight separators. Nucl. Instrum. Methods Phys. B **266**, 4657 (2008). https://doi.org/10.1016/j.nimb.2008.05.110

31. LISE++. https://lise.nscl.msu.edu/lise.html

32. S. Agostinelli et al., Geant4—a simulation toolkit. Nucl. Instrum. Methods Phys. A **506**(3), 250–303 (2003). https://doi.org/10.1016/S0168-9002(03)01368-8

33. J. Allison et al., Geant4 developments and applications. IEEE Trans. Nucl. Sci. **53**(1), 270–278 (2006). https://doi.org/10.1109/TNS.2006.869826

34. J. Allison et al., Recent developments in Geant4. Nucl. Instrum. Methods Phys. A **835**, 186–225 (2016). https://doi.org/10.1016/j.nima.2016.06.125

35. G.F. Song et al., Production and properties of a charging-up "Free" THGEM with DLC coating. Nucl. Instrum. Methods Phys. A **966**, 163868 (2020). https://doi.org/10.1016/j.nima.2020.163868

36. M. Li et al., Exploration of grid scheme for Frisch-grid ionization chamber. Eur. Phys. J. C **81**, 1089 (2021). https://doi.org/10.1140/epjc/s10052-021-09879-y

37. T.L. Qiu et al., New trapezoid-shaped Frisch-grid ionization chamber for low-energy particle measurements. Eur. Phys. J. C **82**, 975 (2022). https://doi.org/10.1140/epjc/s10052-022-10953-2

38. COMSOL Multiphysics. http://www.comsol.com/

39. H.R. Yang et al., Arc field cage manufacturing device and operation method thereof (2022). CN. Patent No. 202110214733.5. https://patentscope2.wipo.int/search/en/detail.jsf?docPN=CN113038727

40. T.-Miki et al., Zigzag-shaped pads for cathode readout of a time projection chamber. Nucl. Instrum. Methods Phys. A **236**, 64–68 (1985). https://doi.org/10.1016/0168-9002(85)90127-5

41. B. Azmoun et al., Design studies for a TPC readout plane using zigzag patterns with multistage GEM detectors. IEEE Trans. Nucl. Sci. **65**(7), 1416–1423 (2018). https://doi.org/10.1109/TNS.2021.3132946

42. B. Azmoun et al., Design studies of high-resolution readout planes using Zigzags with GEM detectors. IEEE Trans. Nucl. Sci. **67**(8), 1869–1876 (2020). https://doi.org/10.1109/TNS.2020.3001847

43. C. Perez-Lara et al., A comparative study of straight-strip and zigzag-interleaved anode patterns for MPGD readouts. IEEE Trans. Nucl. Sci. **69**(1), 50–55 (2022). https://doi.org/10.1109/TNS.2021.3132946

44. E.C. Pollacco et al., GET: a generic electronics system for TPCs and nuclear physics instrumentation. Nucl. Instrum. Methods Phys. A **887**, 81–93 (2018). https://doi.org/10.1016/j.nima.2018.01.020

45. C. Li et al., An optical fiber-based flexible readout system for micro-pattern gas detectors. J. Instrum. **13**, P04013 (2018). https://doi.org/10.1088/1748-0221/13/04/P04013

46. N. Nacereddine, A.B. Goumeidane, Asymmetric Generalized Gaussian Distribution Parameters Estimation based on Maximum Likelihood, Moments and Entropy, 2019 IEEE 15th International Conference on Intelligent Computer Communication and Processing (ICCP), Cluj-Napoca, Romania, pp. 343–350 (2019). https://doi.org/10.1109/ICCP48234.2019.8959693

47. H. Wen et al., Laser test of the prototype of CEE time projection chamber. Nucl. Sci. Tech. **29**, 41 (2018). https://doi.org/10.1007/s41365-018-0382-4

48. Z.Y. Yuan et al., Performance of TPC detector prototype integrated with UV laser tracks for the circular collider. Nucl. Instrum. Methods Phys. A **1040**, 167241 (2022). https://doi.org/10.1016/j.nima.2022.167241

49. Q-smart (450 mJ). https://www.quantel-laser.com/en/products/item/q-smart-450-mj-.html

50. Garfield++. https://garfieldpp.web.cern.ch/garfieldpp/

51. S.F. Biagi, Monte Carlo simulation of electron drift and diffusion in counting gases under the influence of electric and magnetic fields. Nucl. Instrum. Methods Phys. A **421**, 234–240 (1999). https://doi.org/10.1016/S0168-9002(98)01233-9

52. R.K. Carnegie et al., Resolution studies of cosmic-ray tracks in a TPC with GEM readout. Nucl. Instrum. Methods Phys. A **538**, 372–383 (2005). https://doi.org/10.1016/j.nima.2004.08.132

53. J.Y. Xu et al., Performance of a small AT-TPC prototype. Nucl. Sci. Tech. **29**, 97 (2018). https://doi.org/10.1007/s41365-018-0437-6

54. FTFP_BERT. https://geant4-userdoc.web.cern.ch/UsersGuides/PhysicsListGuide/html/reference_PL/FTFP_BERT.html